

Geophysical Research Letters[®]



RESEARCH LETTER

10.1029/2025GL116451

Special Collection:

Holocene climate changes:
process, mechanism and impacts

Key Points:

- A dynamically consistent spatiotemporal evolution of the ASM precipitation was reconstructed using paleoclimate data assimilation
- Precipitation peaked in EH over SA, northern and southern China, but in LH over central China with a continental-wide enrichment of $\delta^{18}\text{O}_\text{c}$
- This variation is dominated by low-latitude solar radiation changes induced by orbital parameters through southward westerly jet shift

Supporting Information:

Supporting Information may be found in the online version of this article.

Correspondence to:

Z. Liu, J. Liu and L. Wan,
liu.7022@osu.edu;
jliu@njnu.edu.cn;
wanlingfeng_123@163.com

Citation:

Ning, L., Xing, F., Liu, Z., Liu, J., Mann, M. E., Wu, F., et al. (2025). Mega-tripolar precipitation change accompanying water isotopes in Holocene Asian Summer Monsoon reanalysis. *Geophysical Research Letters*, 52, e2025GL116451. <https://doi.org/10.1029/2025GL116451>

Received 13 APR 2025

Accepted 18 AUG 2025

Author Contributions:

Conceptualization: Liang Ning, Zhengyu Liu

Formal analysis: Liang Ning, Fangmiao Xing, Fen Wu, Lili Lei







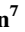

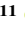






Funding acquisition: Liang Ning, Zhengyu Liu, Jian Liu

Investigation: Mi Yan

© 2025. The Author(s).

This is an open access article under the terms of the [Creative Commons Attribution-NonCommercial-NoDerivs License](#), which permits use and distribution in any medium, provided the original work is properly cited, the use is non-commercial and no modifications or adaptations are made.

Mega-Tripolar Precipitation Change Accompanying Water Isotopes in Holocene Asian Summer Monsoon Reanalysis

Liang Ning¹ , Fangmiao Xing¹ , Zhengyu Liu² , Jian Liu^{1,3} , Michael E. Mann⁴, Fen Wu¹, Lili Lei^{5,6} , Yongjin Wang¹ , Lingfeng Wan⁷ , Hai Xu^{8,9} , Liangcheng Tan^{10,11} , Raymond S. Bradley¹², Mi Yan¹ , Weiyi Sun¹ , Deliang Chen¹³ , Huayu Lu¹⁴ , Qin Wen¹, Kefan Chen¹ , and Yanmin Qin¹ 

¹State Key Laboratory of Climate System Prediction and Risk Management, Key Laboratory for Virtual Geographic Environment, Ministry of Education, State Key Laboratory Cultivation Base of Geographical Environment Evolution and Regional Response of Jiangsu Province, Jiangsu Center for Collaborative Innovation in Geographical Information Resource Development and Application, School of Geography, Nanjing Normal University, Nanjing, China, ²Department of Geography, The Ohio State University, Columbus, OH, USA, ³Jiangsu Provincial Key Laboratory for Numerical Simulation of Large Scale Complex Systems, School of Mathematical Science, Nanjing Normal University, Nanjing, China, ⁴Department of Earth and Environmental Science, Annenberg School for Communication, University of Pennsylvania, Philadelphia, PA, USA, ⁵Key Laboratory of Mesoscale Severe Weather, Ministry of Education, and School of Atmospheric Sciences, Nanjing University, Nanjing, China, ⁶Frontiers Science Center for Critical Earth Material Cycling, Nanjing University, Nanjing, China, ⁷Frontier Science Center for Deep Ocean Multispheres and Earth System, Institute for Advanced Ocean Study and Key Laboratory of Physical Oceanography, Ministry of Education, Ocean University of China, Qingdao, China, ⁸Key Laboratory of Karst Georesources and Environment, Ministry of Education, College of Resources and Environmental Engineering, Guizhou University, Guiyang, China, ⁹School of Earth System Science, Institute of Surface-Earth System Science, Tianjin University, Tianjin, China, ¹⁰State Key Laboratory of Loess, Institute of Earth Environment, Chinese Academy of Sciences, Xi'an, China, ¹¹Institute of Global Environmental Change, Xi'an Jiaotong University, Xi'an, China, ¹²Department of Earth, Geographic, and Climate Sciences, Climate System Research Center, University of Massachusetts Amherst, Amherst, MA, USA, ¹³Department of Earth System Sciences, Tsinghua University, Beijing, China, ¹⁴School of Geography and Ocean Science, Nanjing University, Nanjing, China

Abstract The climatic interpretations of speleothem $\delta^{18}\text{O}_\text{c}$ records over Asian summer monsoon (ASM) region have been controversial. Here, combining speleothem $\delta^{18}\text{O}_\text{c}$ records with the first transient Holocene simulation of an isotope-enabled earth system model, we reconstruct a dynamically consistent spatio-temporal evolution of the ASM precipitation using paleoclimate data assimilation. Our reconstruction finds a new mega-tripolar pattern of precipitation variations accompanying a continental-wide enrichment of $\delta^{18}\text{O}_\text{c}$ from the early to late Holocene over the entire ASM continental region. Precipitation peaked in the early Holocene over South Asia, northern China and southern China, but in the late Holocene over central China. This mega-tripolar pattern of precipitation variations can help resolve the long-standing controversy about the timing of Holocene ASM precipitation peaks reconstructed from various proxy records.

Plain Language Summary By assimilating speleothem $\delta^{18}\text{O}_\text{c}$ records with the first transient Holocene simulation of an isotope-enabled Earth system model, we reconstruct the dynamically consistent spatio-temporal evolution of ASM precipitation. This Holocene ASM reanalysis reveals a newly identified mega-tripolar pattern in precipitation changes, along with a widespread $\delta^{18}\text{O}_\text{c}$ enrichment from the early to late Holocene across the whole ASM region. Notably, precipitation peaked in the early Holocene over South Asia to both northern and southern China, but shifted to central China during the late Holocene.

1. Introduction

The Asian summer monsoon (ASM) system is dominated by a summer precipitation spanning from the South Asia (SA) to the East Asia (EA), strong southwesterly low level monsoon wind, high surface moist static energy (MSE) and depleted stable water isotopes in precipitation $\delta^{18}\text{O}_\text{p}$, and mid-latitude westerly jet at 200 hPa (Figures 1a and 1b). The ASM precipitation is vital to over half of the world population, yet its response to external climate forcing remains unclear. Notably, the timing of Holocene ASM rainfall maximum across regions—the “Time-transgressive Holocene Optimum issue”—has remained an outstanding issue (An et al., 2000; W. Zhou, 2004). Early modeling suggested a weakened summer monsoon intensity after early-to-middle Holocene simply across the Afro-Asian monsoon region due to decreasing summer insolation

Methodology: Liang Ning, Fangmiao Xing, Zhengyu Liu, Fen Wu, Lili Lei, Yongjin Wang, Lingfeng Wan
Software: Lili Lei, Lingfeng Wan
Supervision: Zhengyu Liu, Jian Liu, Michael E. Mann, Raymond S. Bradley, Huayu Lu
Validation: Liang Ning
Writing – original draft: Liang Ning, Zhengyu Liu
Writing – review & editing: Liang Ning, Fangmiao Xing, Zhengyu Liu, Jian Liu, Michael E. Mann, Lili Lei, Yongjin Wang, Lingfeng Wan, Hai Xu, Liangcheng Tan, Raymond S. Bradley, Mi Yan, Weiye Sun, Deliang Chen, Huayu Lu, Qin Wen, Kefan Chen, Yanmin Qin

(COHMAP et al., 1988; Kutzbach & Otto-Bliesner, 1982). Proxy data over the South Asia summer monsoon (SASM) region supports this, but large uncertainty persists in EA. For example, An et al. (2000) first proposed a southward delay in EA rainfall maximum from ~10 ka BP in north China to ~3 ka BP in the south, a.k.a. “the asynchronous Holocene Optimum,” a pattern also seemingly consistent with recent fossil pollen records (Herzschuh et al., 2019). However, other studies present contrasting results: a synchronous rainfall maximum at ~10 ka BP across the entire EASM region (W. Zhou et al., 2007), a transgressive pattern with northward shift in the early Holocene followed by a southward shift in the late Holocene (Ran & Feng, 2013), or a northward transgressive pattern of the Holocene rainfall maximum from southern China (~10 ka BP) to northeastern China (~6 ka BP) (X. Zhou et al., 2022, 2023).

These divergent views reflect complex mechanisms, involving southward progressive weakening of solar radiation (An et al., 2000), peak in Northern Hemisphere solar insolation (W. Zhou et al., 2007), delayed low-latitude oceanic warming (Ran & Feng, 2013), shift in the western Pacific subtropical high (WPSH) (X. Zhou et al., 2022), and a role of vegetation feedbacks (Cheng et al., 2021). Specifically, the shift from northwest to southeast is interpreted as ASM progressive weakening in response to decreasing summer solar radiation related to orbital forcing (An et al., 2000). The synchronous rainfall maximum in both northern and southern China are considered to be consistent with global pattern in response to changes in Northern Hemisphere solar radiation, rather than simply a local expression (W. Zhou et al., 2007). The lag response of low-latitude oceans to peak summer insolation, which was then reflected in southern China also with some time lags, resulting gradual northward EASM transgression in early Holocene and southward transgression in late Holocene (Ran & Feng, 2013). While, low-latitude monthly insolation changes rather than average summer insolation changes, are considered as the main forcing of northward transgression through WPSH shift (W. Zhou et al., 2022). These contradictory studies on the reconstruction and mechanism pose a great challenge in our understanding of the ASM precipitation response to external forcing (X. Zhou et al., 2016).

One major challenging is the lack of reliable regional moisture proxy records in the central and southern China. Moreover, lack of Holocene $\delta^{18}\text{O}$ -enabled transient simulations also poses additional difficulties to resolve this discrepancy. Among various moisture proxy records, speleothem $\delta^{18}\text{O}_c$ records show the most robust Holocene variations over entire ASM region, showing an enriching trend after the early Holocene peak (H. Cheng et al., 2009; Y. L. Wang, 2001; Yuan et al., 2004), reflecting dynamic links between $\delta^{18}\text{O}_p$ and precipitation (Pausata et al., 2011; Z. Liu, 2014). As the first $\delta^{18}\text{O}$ -enabled transient modeling, iTraCE enables direct comparison on Holocene ASM evolution between model simulations and proxy records, and also improves understanding on the climatic representation of $\delta^{18}\text{O}$. It can capture ASM responses to different time-varying forcings, and reflect multiple scale dynamics. Here, combining speleothem $\delta^{18}\text{O}_c$ records (Chiang et al., 2020; Clemens et al., 2010; Q. Wen et al., 2024) with iTraCE simulations through paleoclimate data assimilation (PDA), we reconstruct the pattern of Holocene ASM precipitation variation, revealing a uniform $\delta^{18}\text{O}_c$ enriching pattern but regionally inhomogeneous precipitation response, characterized by a mega-tripolar precipitation pattern over central China. This reconstruction is used to give the optimal estimate of the Holocene ASM precipitation evolution, which is consistent with both speleothem $\delta^{18}\text{O}_c$ records and iTraCE simulation within their uncertainties.

2. Data and Methods

2.1. Data

iTraCE simulation (Otto-Bliesner et al., 2024) is performed by the water isotope-enabled version of the Community Earth System Model version 1.3 (iCESM1.3), which could capture the observed variations of $\delta^{18}\text{O}_p$ and δD in the atmosphere, land, ocean, and sea ice (Brady et al., 2019; Stevenson et al., 2019). The iTraCE transient simulations enable the most comprehensive model-data comparison study since LGM, which shows skilled performances on analyses of the global and regional precipitation and $\delta^{18}\text{O}_p$ variations (He et al., 2021a, 2021b, 2021c).

The experimental design largely follows the previous TraCE-21ka experiment (Z. Liu et al., 2009). The external forcings include the ice sheet (ICE-6G) and ocean bathymetry (Peltier et al., 2015), orbital parameters (Berger, 1978), greenhouse gas concentrations (Lüthi et al., 2008), and melting water flux (Figure 2a). For now, there is only one baseline experiment (ICE + ORB + GHG + MWF) covering the whole Holocene accomplished. The iTraCE Holocene simulation was branched from the iTraCE LIG simulation at 11 ka BP. During the

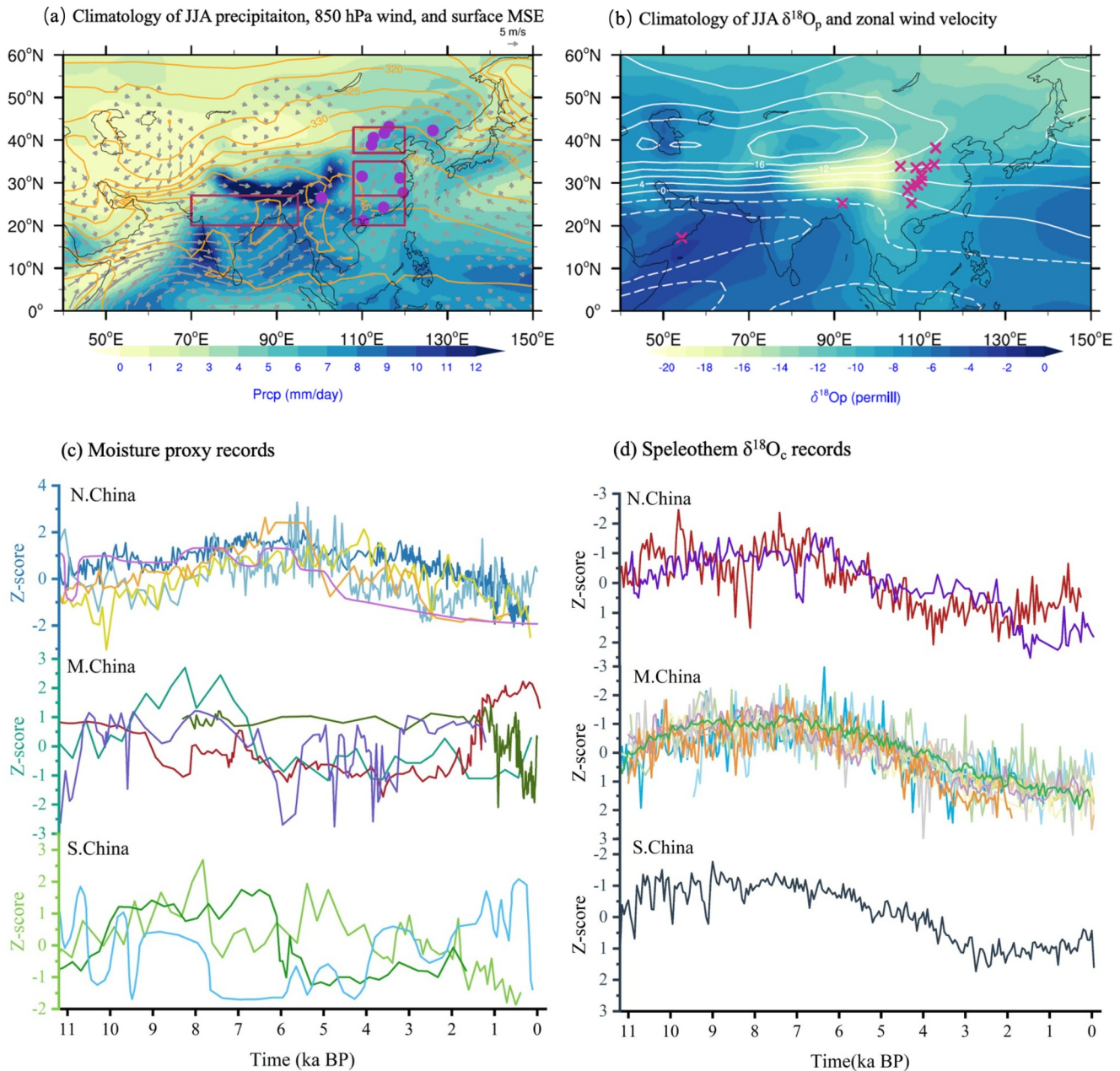


Figure 1. Climatology of iTraCE hydroclimate variables during the Holocene and EASM variations shown in proxy records. (a) Model summer [June, July, August (JJA)] precipitation (Prcp, shading), 850-hPa wind (vector), and surface MSE (contours, in K) with sites of moisture proxy records marked as purple dots. (b) $\delta^{18}\text{O}_p$ (shading) and zonal wind velocity averaged between 500 and 200 hPa (contour, solid for positive and dash for negative) with sites of speleothem $\delta^{18}\text{O}_e$ records marked as red crosses. In (a), red boxes mark the regions of northern China (N. China, 37–43°N, 108–120°E), central eastern China (C. China, 27–35°N, 108–120°E), southern China (S. China, 20–27°N, 108–120°E), and South Asia (S. Asia, 20–27°N, 70–95°E) in Figures 2b–2d, respectively. (c) Normalized reconstructed pollen record (yellow) at Sihailongwan Lake (Stebich et al., 2015), pollen record (orange) at Bayanchagan Lake (W. Jiang et al., 2006), reconstructed precipitation (dark blue) at Gonghai Lake (Chen et al., 2015), reconstructed precipitation (light blue) at Daihai Lake (Xiao et al., 2004), reconstructed lake level (purple) at Dali Lake (Goldsmith et al., 2017) over northern China; the precipitation proxy (chemical index of alteration) for Nanyi Lake (red) (J. Liu et al., 2020), pollen record (forest green) at Dajuhu Peatland (C. Zhu et al., 2010), mass accumulation rate of aerobic hopanoids (Xie et al., 2013), pollen record (dark green) at Wangdongyang Peatland (Zhao et al., 2021) over the central eastern China; pollen record (green) at Dahu Peatland (Z. Zhou, 2004), reconstructed lake level (light blue) at Chenghai Lake (Xu et al., 2020), and pollen record (light green) at Huangguangyan Maar Lake (S. Wang et al., 2007). Detailed information in Table S1 in Supporting Information S1. (d) Normalized reconstructed speleothem $\delta^{18}\text{O}_e$ records at Lianhua and Zhenzhu Caves over northern China, Wuya, Magou, Heshang, Sanbao, Shigao, Jiuxian, Furong, Luoshui, Lianhua, Xiniu, and Dongshiya Caves over central eastern China, and Dongge cave over southern China. Detailed information in Table S2 in Supporting Information S1.

simulation, continental ice sheets were modified at 10, 9, 8.5, 7, and 6 ka, based on the ICE-6G reconstruction. The land-sea configurations were changed at 10, 8.5, 8.4, 7, and 6 ka. From 6 to 0 ka, both continental ice sheet and land-sea configuration are set to the PI conditions and remain unchanged.

Twelve moisture proxy records (detailed information in Text S1 in Supporting Information S1) are used for comparison with simulated and assimilated results. Reconstructed level changes of 30 lakes (Yu et al., 2001) are also used to validate assimilated precipitation changes (detailed information in Text S1 in Supporting Information S1). Sixteen speleothem $\delta^{18}\text{O}$ records dispersing the ASM region from the SISAL2.0 archive (Comas-Bru, Atsawawanunt, et al., 2020; Comas-Bru, Rehfeld, et al., 2020) are used for PDA, and their information and pre-processing procedures are shown in Text S2 in Supporting Information S1.

2.2. Methods

The paleoclimate data assimilation method used in this study is the offline ensemble Kalman filter (EnKF), which has been widely used to reconstruct the paleoclimate of the last millennium, Holocene, and LGM (Erb et al., 2022; Tardif et al., 2019; Tierney et al., 2020). The basic idea of offline EnKF is to calculate the ensemble of posterior climate states (x_a) from proxy data records (y) and prior climate states from model simulations (x_b):

$$x_a = x_b + K(y - y_e) \quad (1)$$

The EnKF method comprises four main components: proxy records, which provide indirect records of past climate variables; climate models, which provide prior estimates of climate variabilities with the original temporal resolution (i.e., decadal resolution in this study); and proxy system models (PSMs), which establish relationships between model priors and proxy records; and the ensemble Kalman filter operator, which estimates climate variables through a weighted average of the model spatial fields and proxy information. The weights of proxy records and model simulations are quantitatively calculated based on their uncertainties, with smaller weights for large uncertainties (Text S3 in Supporting Information S1), to generate optimal estimate of climate variation from these two data sources.

In assimilation, the prior ensemble of 100 members is randomly drawn from iTraCE Holocene simulations with original decadal resolution. The simulated $\delta^{18}\text{O}_p$ and precipitation serve as prior in this study, and the posterior are also these two variables with the same 50-year resolution consistent with speleothem $\delta^{18}\text{O}_e$ records. The temporal variation of the posterior is derived from the integrated temporal information of proxy records and model simulations, while the spatial covariance relies solely on the model priors. The error variance of the proxy record is estimated as the variance of the regression residuals. The distance-weighted radius defines the farthest area where the proxy record can participate in assimilation. In this article, it is set to 24,000 km, but it is insensitive. The calculation of PSMs and uncertainty are given in Text S4 in Supporting Information S1. The details of validation are shown in Tables S3 and S4 in Supporting Information S1.

3. Results

3.1. Paleoclimate Reconstructions of ASM Variations

Regional syntheses of moisture proxy records (detailed information in Table S1 in Supporting Information S1) show that proxy records over northern China are generally consistent with moisture peaks in the early to middle Holocene, while proxy records over central China and southern China show large uncertainties with no consistent moisture trends in the Holocene, as shown in some typical proxy records in these regions. Over northern China (upper panel of Figure 1c), the pollen record at Sihailongwan Maar Lake (Stebich et al., 2015) shows a Holocene precipitation maximum occurrence in the middle to late Holocene (~4 ka BP), and the pollen record at Bayanchagan Lake (W. Jiang et al., 2006) also shows a Holocene precipitation maximum occurrence at ~6 ka BP. The reconstructed precipitation at Gonghai Lake (Chen et al., 2015) and Daihai Lake (Xiao et al., 2004) shows a maximum in the mid-Holocene, with magnitudes of about 700 and 600 mm, respectively. Reconstructed lake levels at Dali Lake (Goldsmith et al., 2017) show a Holocene precipitation maximum occurrence in early to middle Holocene (10–6 ka BP). In comparison, over central China (middle panel of Figure 1c), tree pollen in Dajuhu Peat (C. Zhu et al., 2010) shows a Holocene precipitation maximum from 9–7 ka BP, in contrast with the mid-Holocene dry interval shown in the chemical index of alteration (CIA) record at Nanyi Lake (J. Liu et al., 2020) and the mass accumulation rate of aerobic hopanoids (Xie et al., 2013). Over southern China (lower

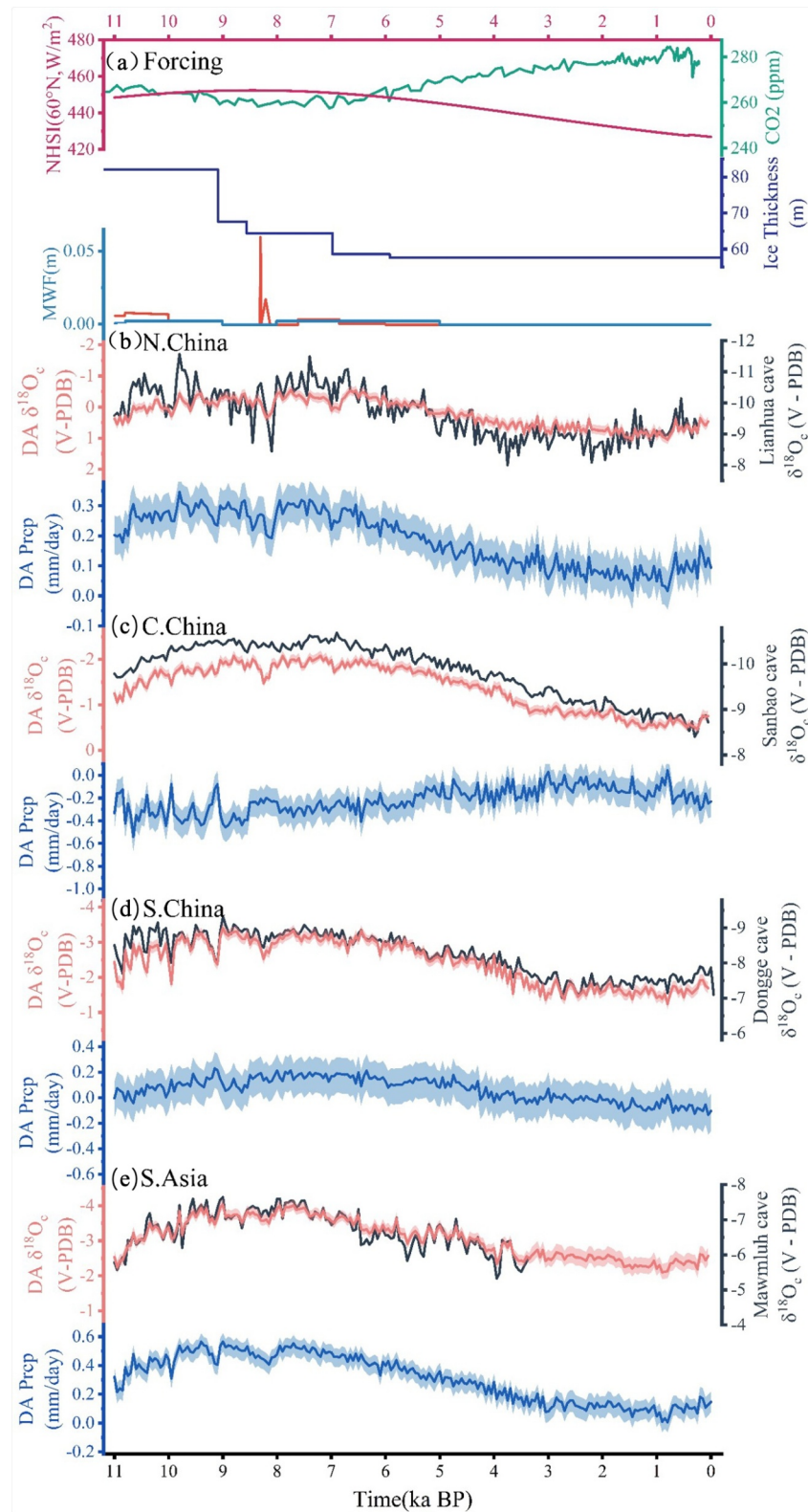


Figure 2.

panel of Figure 1c), the tree pollen records at Huangguangyan Maar Lake (S. Wang et al., 2007) and Dahu Peat (Z. Zhou, 2004) show similar Holocene peak rainfall occurrences in the early Holocene, similar to northern China. However, reconstructed lake level at Chenghai Lake (Xu et al., 2020) shows a mid-Holocene low lake level, but high lake levels in the early and late Holocene. The ratios of uncertainty over trend, defined as the spread of proxy records over the Holocene variation within each region, are 34.21%, 59.59%, and 52.90%, respectively. The records are plotted together here to show uncertainties among moisture proxy records within each region (Figure 1c), and they are plotted in separate lines in Figure S6a in Supporting Information S1.

It is noteworthy that all the pollen records in the three regions show a similar peak in the early Holocene (Figure 1c). This may indicate that these pollen records show similar vegetation responses to the northern hemisphere summer solar insolation maximum, but with different climate interpretations. The pollen records over northern China may represent the precipitation variations, while those over the other two regions may reflect temperature variations.

In contrast to these moisture proxy records, the speleothem isotope $\delta^{18}\text{O}_c$ records from 16 caves over all three regions (Table S2 in Supporting Information S1) show a highly consistent change with the early Holocene peak of depletion (Figure 1d and Figure S3 in Supporting Information S1). This difference raised several key questions, for example, what was the EASM precipitation pattern during the Holocene? Are the climatic interpretations of these moisture proxy records correct? To what extent can the speleothem isotope $\delta^{18}\text{O}_c$ records represent the EASM precipitation variations? These questions will be discussed through the investigation of assimilated precipitation, derived with the aid of climate dynamics within the isotope-enabled transient simulation.

3.2. Paleoclimate Simulation and Data Assimilation of ASM $\delta^{18}\text{O}$ -Hydroclimate

The iTraCE simulation provides a unique opportunity for comprehensive data-model comparisons between $\delta^{18}\text{O}$ and associated hydroclimate changes over the ASM region during the Holocene. It also provides the dynamical constraint that is critical to assimilate precipitation through observed $\delta^{18}\text{O}_c$ records directly. The paleoclimate data assimilation product is used to give the optimal estimate of the precipitation variation, which is consistent with both proxy records and model simulation within their uncertainties. The $\delta^{18}\text{O}_c$ records from 16 caves over the Asia monsoon regions (Figure 1b) are used in this procedure, and their detailed information is shown in Table S2 in Supporting Information S1. The timing and magnitude of Holocene precipitation over ASM region is then investigated through detailed comparison between model simulation, data assimilation, and observed $\delta^{18}\text{O}_c$ records.

To assess the reliability of assimilated results, we compare the assimilated $\delta^{18}\text{O}_c$ (derived from the $\delta^{18}\text{O}_p$, details in Text S5 in Supporting Information S1) to independent speleothem $\delta^{18}\text{O}_c$ records, following Tierney et al. (2020). In this step, 25% of the speleothem $\delta^{18}\text{O}_c$ records (4 caves) were randomly withdrawn from the PDA, and used for validation, repeated for five times. Furthermore, to avoid potential inflation of validation statistics, if one independent speleothem $\delta^{18}\text{O}_c$ record is within $3^\circ \times 3^\circ$ grid cell of any record used in assimilation, it is removed from the validation. Overall, 68% of the variance in observed $\delta^{18}\text{O}_c$ changes between the early, middle and late Holocene can be explained by the assimilated $\delta^{18}\text{O}$ results (Figure S1a in Supporting Information S1), compared with only 1% of the variance in observed $\delta^{18}\text{O}_c$ changes explained by the prior (Figure S1b in Supporting Information S1). The assimilated $\delta^{18}\text{O}_c$ changes share 3% of the variance with the simulated $\delta^{18}\text{O}_c$ changes (Figure S1c in Supporting Information S1). This suggests that the assimilation reproduces $\delta^{18}\text{O}_c$ changes through the Holocene more consistent with the observation than the pure model simulation (68% vs. 1%), a conclusion that can also be derived from the comparison individually across the 16 caves (Figure S2 in Supporting Information S1). Notably, the magnitude of the $\delta^{18}\text{O}_c$ variation in the Holocene is much smaller in the prior fields (simulation) than in observations, and this deficiency is largely improved by the assimilation, such that the

Figure 2. Hydroclimate- $\delta^{18}\text{O}$ evolution in iTraCE, assimilation, and observation. (a) Forcing: atmospheric CO_2 concentration (green), June insolation at 60°N (red), ice sheet thickness (dark blue), and meltwater fluxes in the northern (red) and southern (blue) Hemisphere. (b) Observed calcite $\delta^{18}\text{O}_c$ (black) and assimilated $\delta^{18}\text{O}_c$ (orange) at Lianhua Cave, and assimilated annual precipitation (blue) in northern China ($37\text{--}43^\circ\text{N}$, $108\text{--}120^\circ\text{E}$). (c) Observed calcite $\delta^{18}\text{O}_c$ (black) and assimilated $\delta^{18}\text{O}_c$ (orange) at Sanbao Cave, and assimilated annual precipitation (blue) in central eastern China ($27\text{--}35^\circ\text{N}$, $108\text{--}120^\circ\text{E}$). (d) Observed calcite $\delta^{18}\text{O}_c$ (black) and assimilated $\delta^{18}\text{O}_c$ (orange) at Dongge Cave, and assimilated annual precipitation (blue) in southern China ($20\text{--}27^\circ\text{N}$, $108\text{--}120^\circ\text{E}$). (e) Observed calcite $\delta^{18}\text{O}_c$ (black) and assimilated $\delta^{18}\text{O}_c$ (orange) at Mawmluh Cave, and assimilated annual precipitation (blue) in South Asia ($20\text{--}27^\circ\text{N}$, $70\text{--}95^\circ\text{E}$). All the simulated results have been smoothed with a 50-year running mean.

assimilated $\delta^{18}\text{O}_c$ show magnitudes much closer to the observed records than the model simulation alone (Figure S3 in Supporting Information S1). This weak $\delta^{18}\text{O}_c$ response to orbital forcing seems to be a common deficiency in current climate models, in spite of reasonable seasonal cycle response as in present day observations (Battisti et al., 2014; Z. Liu, 2014; Tabor et al., 2018; X. Wen et al., 2016). Here, by assimilating the observed $\delta^{18}\text{O}_c$ signal, the reconstructed climate evolution integrates both the observational $\delta^{18}\text{O}_c$ signal and model covariance between $\delta^{18}\text{O}_c$ and climate variables (e.g., precipitation and winds), reproducing climate variability consistent with the observations and model simulations within their uncertainties. The assimilated precipitation changes are also consistent with reconstructed lake level changes of 30 lakes across China (Figure S4 in Supporting Information S1).

3.3. Holocene ASM $\delta^{18}\text{O}$ -Hydroclimate Evolution

The assimilated hydroclimate evolution in the Holocene exhibit distinct features (Figure 2). In northern China, the assimilated $\delta^{18}\text{O}_c$ captures the major feature of the observation $\delta^{18}\text{O}_c$ at Lianhua Cave, with a large enrichment from the early and mid-Holocene toward late Holocene (Figure 2b). The magnitude of observed $\delta^{18}\text{O}_c$ variation in the Holocene is about 3‰ (−11.5‰ to −8.5‰). The assimilated $\delta^{18}\text{O}_c$ variation is similar to the observation, with a smaller enrichment of about 2‰. The assimilated precipitation peaks around the early to mid-Holocene, somewhat similar to that in the simulation (Figure S5 in Supporting Information S1) but with a greater magnitude than in the simulation (0.3 mm/day vs. 0.2 mm/day). This largely decrease of precipitation toward late Holocene in the DA analysis is overall consistent with the robust change across various moisture proxies there (Figure 2c, top). The enrichment of $\delta^{18}\text{O}_c$ and the decreased precipitation appears in the same sign as the nominal “amount effect.”

In central China, the $\delta^{18}\text{O}_c$ at Sanbao Cave shows maximum depletion in the early to mid-Holocene and a strong enrichment trend toward late Holocene, with a magnitude of ~2‰ (−8.5‰ to −10.5‰) (Figure 2c). The assimilated $\delta^{18}\text{O}_p$ captures this enrichment trend of about 2‰. The assimilated precipitation shows, however, an increasing trend through the Holocene (Figure 2c), similar to the simulation (Figure S5 in Supporting Information S1). This increase in precipitation alongside $\delta^{18}\text{O}_c$ enrichment is opposite to the local “amount effect,” as noted in previous multiproxy speleothem study (Zhang et al., 2018), potentially indicating shift of moisture source regions.

In southern China, similar to northern China, the observed $\delta^{18}\text{O}_c$ at Dongge Cave shows enrichment from the early and mid-Holocene to the late Holocene (Figure 2d). The assimilated $\delta^{18}\text{O}_c$ shows a similar ~2‰ enrichment. The assimilated precipitation decreases, again consistent with the local “amount effect.”

In the SA, the observed $\delta^{18}\text{O}_c$ at Mawmluh Cave shows ~2‰ enrichment in the Holocene (Figure 2e), similar to that in China. The assimilated $\delta^{18}\text{O}_c$ matches this, with precipitation decreasing toward the late Holocene by ~0.5 mm/day, consistent with the iTraCE simulation (Figure S2 in Supporting Information S1) and previous studies (Kutzbach & Otto-Bliesner, 1982). The changes in $\delta^{18}\text{O}_c$ and precipitation are consistent with the “amount effect.”

In summary, the assimilated $\delta^{18}\text{O}_c$ exhibit a common enrichment trend in the Holocene over the entire Asia monsoon region, while the assimilated precipitation decreases over the northern and southern China as well as SA, but increases in central China.

3.4. Mega-Tripolar Pattern of the Holocene ASM Precipitation Variation

The assimilated precipitation is then compared with the moisture proxy records to investigate the timing of EASM Holocene precipitation maximum (Figure S6 in Supporting Information S1). Over northern China, the assimilated precipitation Dali Lake, Sihailongwan Lake, Bayanchagan Lake, and Daihai Lake show maximum precipitation in the early-to-mid Holocene, and then decrease through the late Holocene. Over central China, assimilated precipitation shows an increasing trend through the Holocene, consistent only with the record from Nanyi Lake. Over southern China, the early Holocene maximum in tree pollen at Huangguangyan Maar Lake and Dahu Peat is also consistent with the assimilated precipitation. So, the observations and assimilated results both indicate early Holocene precipitation maximum over northern and southern China, and a late Holocene maximum over central China, forming a mega-tripolar pattern. This “mega-tripolar” pattern is different from typical tripolar pattern over EASM region discussed in previous studies (e.g., Zhang et al., 2018), because it also extends to SA (Figure S7 in

Supporting Information S1). The regional precipitation variations from assimilation are consistent with reconstructed precipitation and lake level records (Figure S6 in Supporting Information S1).

This mega-tripolar pattern is further evident in the spatial distribution of the Holocene precipitation maximum. Assimilated $\delta^{18}\text{O}_c$ (Figure S7a in Supporting Information S1) shows an early Holocene maximum ($\sim 8\text{--}10$ ka BP) across SA to EASM regions, consistent with observed $\delta^{18}\text{O}_c$ over eastern China and SA (Figure 2). Assimilated precipitation shows the Holocene maximum in the early Holocene ($\sim 8\text{--}10$ ka BP) across SA and northern China, but in the late Holocene over central China (Figure S7b in Supporting Information S1). The northern early Holocene maximum mode within this pattern is also consistent with the early Holocene maximum at ~ 8 ka BP over the margin of the EASM region, based on eolian dust and pollen records (X. Zhou et al., 2023) as well as lake level reconstructions (Goldsmith et al., 2017; M. Jiang et al., 2020). Precipitation changes from early to late Holocene are about -10% over northern and southern China, and 10% over central China (Figure S7c in Supporting Information S1), with standard deviations of $\sim 6\%\text{--}8\%$ across eastern China (Figure S7d in Supporting Information S1). Furthermore, the early Holocene precipitation maximum over southern China extends to southwestern China, consistent with the Indian monsoon maximum (An et al., 2000) and high lake levels during the early Holocene (Z. Liu, 2014).

Although, this early Holocene precipitation maximum in northern China and southern China is partially consistent with An et al. (2000) and X. Zhou et al. (2023), no time-transgressive pattern through the whole of eastern China in the data assimilation. Instead, a sharp contrast in the late Holocene precipitation maximum in central China, showing an obvious mega-tripolar pattern, similar to the EASM precipitation pattern in both paleoclimate and modern climate (Ning et al., 2017; Zhang et al., 2018). The similar early Holocene maximum depletion in $\delta^{18}\text{O}_p$ over eastern China and precipitation over northern China suggests $\delta^{18}\text{O}_p$ variations represent EASM strength and corresponding northern precipitation (Z. Liu, 2014). Therefore, this pattern differs from previous interpretations of a southward time-transgressive rainfall maximum (An et al., 2000) or gradual northward migration driven by insolation changes (X. Zhou et al., 2022). Moreover, the assimilated precipitation over northern and southern China aligns with multiple proxy records, while over central China, where proxies vary, the assimilation provides a more dynamically reasonable benchmark for Holocene precipitation reconstructions.

3.5. Large-Scale Circulation Associated With the Mega-Tripolar Holocene Precipitation Maximum Occurrence

To reveal the physical mechanism behind this mega-tripolar Holocene precipitation maximum pattern, we identify the hydroclimate footprint over the whole Asia monsoon region using the leading pattern of the multiple variable empirical orthogonal function (MV-EOF) based on summer $\delta^{18}\text{O}_p$, precipitation, 850 hPa and 200 hPa wind fields on decadal resolution. The leading spatial mode of MV-EOF analysis, explaining 89.6% of the total variance, shows a sub-orbital scale uniform $\delta^{18}\text{O}_p$ variation over EASM region, but the precipitation variations are opposite over SA to northern and southern China and over central China (Figure 3). Tagging experiments (not shown) suggest that the uniform $\delta^{18}\text{O}_p$ pattern mainly results from enhanced moisture contribution from the Indian Ocean. This uniform $\delta^{18}\text{O}_p$ anomaly is negatively correlated with precipitation over SA and northern-southern China, but positively correlated with central China precipitation, consistent with previous modeling (Z. Liu, 2014) and proxy records (Zhang et al., 2018), which associate the depleted $\delta^{18}\text{O}_p$ anomalies over the EASM region with an intensified EASM, inducing enhanced precipitation over northern and southern China but decreased monsoon precipitation over central China. This meridional mega-tripolar pattern is also the dominant mode of decadal-scale EASM precipitation variations in the observations (Ding et al., 2008). This implies that the uniform $\delta^{18}\text{O}_p$ signal effectively represents EASM strength, notably the monsoon southerly wind and precipitation over northern China, although the $\delta^{18}\text{O}_p$ signal over EASM region is significantly impacted by upstream rainout effects along the monsoon moisture trajectory. The leading principal component (PC1) shows a pronounced decreasing trend through the Holocene (Figure 3d), indicating a $\delta^{18}\text{O}_p$ enrichment and declining precipitation over the whole ASM region.

The MV-EOF spatial mode of 200 hPa wind field show mid-latitude easterly wind anomalies associated with positive loading of PC1 (Figure 3a), while 850 hPa winds exhibit southwesterly anomalies over SASM and southerly anomalies over EASM, accompanied by a strengthened WPSH (Figure 3b). This coupled mode of a westerly jet and monsoon circulation favors low-level convergence over the EASM region at

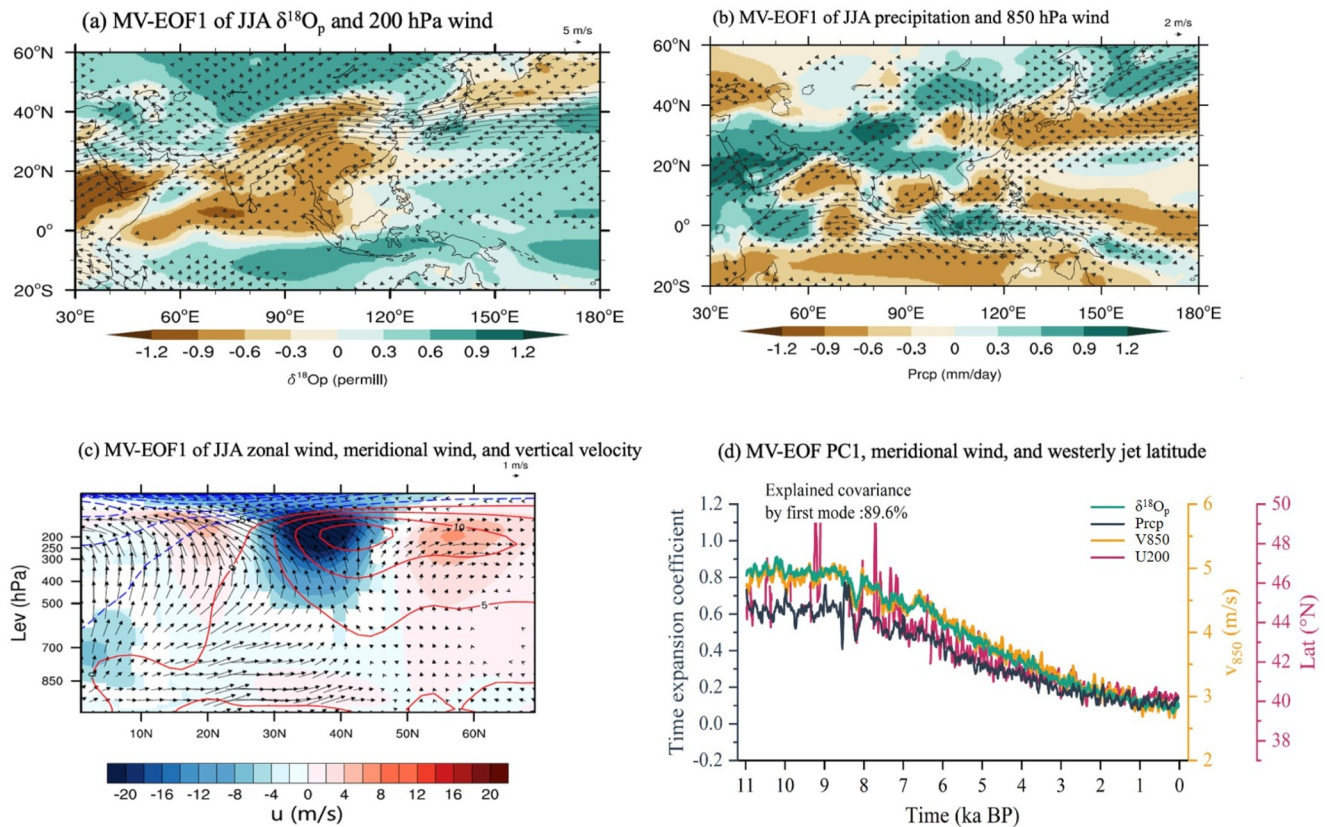


Figure 3. Covariance among Asian summer monsoon $\delta^{18}\text{O}_p$, precipitation, and the accompanying circulation patterns, as illustrated by the first MV-EOF mode between summer (JJA) $\delta^{18}\text{O}_p$ and precipitation over the ASM region in iTraCE. (a) Summer $\delta^{18}\text{O}_p$ (shading) and 200-hPa wind (vector) regressed on the normalized time coefficient of $\delta^{18}\text{O}_p$ (black in (d)). (b) As in (a) but for summer precipitation (shading) and 850-hPa wind (vector). (c) As in (a) but for zonal wind u (shading), meridional wind v , and vertical velocity w (vector) zonally averaged over East Asia (108°E to 120°E). In (c), contours are for climatological u (positive, solid red; negative, dash blue) at Holocene, and w is amplified by a factor of 500 for visualization. (d) Time series of the normalized time coefficients of the first MV-EOF mode (black for $\delta^{18}\text{O}_p$, green for precipitation, in black axis), 850-hPa meridional wind v strength over East Asia (22°N to 43°N, 108°E to 120°E; yellow), 200-hPa westerly jet latitude centroid (red) (108°E to 120°E).

about 20°N–40°N, inducing anomalous ascent motions and convection (Figure 3c). Given the decreasing trend of PC1 (Figure 3d), this indicates a concurrent strengthening of the westerly jet and weakened ASM through the Holocene, with enhanced convection over central China at about 30°N. This is confirmed by the southward shift of the 200-hPa westerly jet latitude centroid and a retreating EASM index, defined as 850-hPa meridional wind strength over East Asia strongly correlated with PC1 (Figure 3d). This megatripolar pattern of precipitation variations is directly induced by weakened monsoon wind, and corresponding moisture divergence over SA to northern China, but moisture convergence over central China (Figure 3b). Similar conclusions could also be drawn from MV-EOF analysis using the assimilated fields (Figure S8 in Supporting Information S1). The eastward-shifted, weakened WPSH and strengthened westerly jet (Figures 3a, 3c, and 3d) further contribute to this pattern (See details in Text S6 in Supporting Information S1). Similar patterns can also be seen over the SA region (See details in Text S7 in Supporting Information S1).

Generally, there is a homogeneous continental-scale negative $\delta^{18}\text{O}_p$ pattern over the whole ASM region, with positive precipitation patterns over SA to northern China and southern China, indicating the amount effect, while the $\delta^{18}\text{O}_p$ -precipitation relationship changes to positive over central China, the Arabian Sea and Bay of Bengal. The opposite precipitation variations between SA and the Arabian Sea and Bay of Bengal indicate that the response of precipitation to the insolation changes induced by orbital parameters is different over land and sea. This coupled hydroclimate- $\delta^{18}\text{O}_p$ response thus forms a distinctive megatripolar Holocene precipitation maximum occurrence pattern, such that early Holocene $\delta^{18}\text{O}_p$ maximum depletion is associated with early-to-mid

Holocene precipitation and soil moisture maximum from SA to northern China and southern China (Figure S5a, S5c, and S5d in Supporting Information S1), but a late Holocene precipitation maximum in central China (Figure S5b in Supporting Information S1), along with a strengthening of the westerly jet and weakened southwesterly monsoon wind.

Different mechanisms have been proposed to explain the several time-transgressive patterns of Holocene precipitation maximum over ASM regions (An et al., 2000; J. Cheng et al., 2021; W. Jiang et al., 2019; X. Zhou et al., 2023). Here, the MV-EOF PC1 and westerly jet strength (Figure 3d) are consistent with the summer insolation variation (Figure 2a), indicating that orbital-driven insolation change is the primary forcing. The ASM system's unique response to Holocene insolation change induces the mega-tripolar precipitation pattern (Figures 3a and 3b), with WPSH weakening and eastward shift caused by decreased summer insolation, and a strengthened westerly jet driven by enhanced equator-to-pole temperature gradients through thermal wind mechanisms.

4. Conclusions and Discussions

In this study, we present a new comprehensive view of the Holocene $\delta^{18}\text{O}_p$ -precipitation variations over the ASM region and answer the long-standing controversy about “Holocene Optimum” occurrence, based on the first isotope-enabled transient model simulations, proxy records, and paleoclimate data assimilations. Our results show that there are different timings of Holocene precipitation maximum over the ASM region, with an early Holocene peak over northern China, southern China and SA but a late Holocene peak over central China. This pattern characterized by a mega-tripolar structure, rather than a gradual transgressive one proposed in previous studies (An et al., 2000; X. Zhou et al., 2023). This spatial pattern is consistent with the $\delta^{18}\text{O}_p$ -precipitation relationship, which reflects the combined effects of upstream rainout and local precipitation amount on continental-scale $\delta^{18}\text{O}_p$ variations (He et al., 2021a). This sub-orbital scale $\delta^{18}\text{O}_p$ -precipitation variation is mainly dominated by low-latitude solar radiation changes induced by the orbital parameters. This mechanism is achieved by the gradual southward westerly jet shift, which is caused by the weakened tropical-polar temperature gradients.

The ASM data assimilation in this study is reasonable because of this dynamically consistent framework, which could improve our understanding of sub-orbital scale variations of hydroclimate- $\delta^{18}\text{O}_p$ over the ASM region, and corresponding physical mechanisms. This also indicates the potential implication of paleoclimate data assimilation to reconstruct the climate of other periods. This mega-tripolar Holocene precipitation maximum variation over ASM regions highlights the complicated circulation and moisture responses to different external forcings, which has implications to improve future ASM projections.

Data Availability Statement

All the assimilated results are publicly available for downloading from Zenodo (Ning et al., 2025). All the speleothem $\delta^{18}\text{O}$ records are downloaded from NOAA Paleoclimatology Data Archive (Comas-Bru, Atsawarant, et al., 2020). The proxy records used for validation are kindly provided by the authors. The iTraCE data are downloaded from the Climate Data Gateway at NCAR (Otto-Bliesner et al., 2024). The Python codes used in this study are publicly available at Zenodo (F. Zhu et al., 2021).

Acknowledgments

We gratefully acknowledge S. Chen for the personal communication about the speleothem oxygen isotope data, and H. Sun for the assistance in implementing data assimilation. This research was jointly supported by the National Key Research and Development Program of China (Grants 2023YFF0804700, 2020YFA0608601), the Science and Technology Innovation Project of Laoshan Laboratory (No. LSKJ202203300), and the National Natural Science Foundation of China (Grants 42130604, 42111530182, 42075049, 42475051, and 42405056).

References

- An, Z. S., Porter, S. C., Kutzbach, J. E., Wu, X. H., Wang, S. M., D Liu, X., et al. (2000). Asynchronous Holocene optimum of the East Asian monsoon. *Quaternary Science Reviews*, 19(8), 743–762. [https://doi.org/10.1016/S0277-3791\(99\)00031-1](https://doi.org/10.1016/S0277-3791(99)00031-1)
- Battisti, D. S., Ding, Q., & Roe, G. H. (2014). Coherent Pan-Asian climatic and isotopic response to orbital forcing of tropical insolation. *Journal of Geophysical Research: Atmospheres*, 119(21), 997–12020. <https://doi.org/10.1002/2014JD021960>
- Berger, A. (1978). Long-term variations of daily insolation and Quaternary climatic changes. *Journal of the Atmospheric Sciences*, 35(12), 2362–2367. [https://doi.org/10.1175/1520-0469\(1978\)035<2362:ltvodi>2.0.co;2](https://doi.org/10.1175/1520-0469(1978)035<2362:ltvodi>2.0.co;2)
- Brady, E., Stevenson, S., Bailey, D., Liu, Z., Noone, D., Nusbaumer, J., et al. (2019). The connected isotopic water cycle in the Community Earth System Model version 1. *Journal of Advances in Modeling Earth Systems*, 11(8), 2547–2566. <https://doi.org/10.1029/2019MS001663>
- Chen, F., Xu, Q., Chen, J., Birks, H. J. B., Liu, J., Zhang, S., et al. (2015). East Asian summer monsoon precipitation variability since the last deglaciation. *Scientific Reports*, 5(1), 11186. <https://doi.org/10.1038/srep11186>
- Cheng, H., Edwards, R. L., Broecker, W. S., Denton, G. H., Kong, X., Wang, Y., et al. (2009). Ice age terminations. *Science*, 326(5950), 248–252. <https://doi.org/10.1126/science.1177840>
- Cheng, J., Wu, H., Liu, Z., Gu, P., Wang, J., Zhao, C., et al. (2021). Vegetation feedback causes delayed ecosystem response to East Asian summer monsoon rainfall during the Holocene. *Nature Communications*, 12(1), 1843. <https://doi.org/10.1038/s41467-021-22087-2>

- Chiang, J. C. H., Herman, M. J., Yoshimura, K., & Fung, I. Y. (2020). Enriched East Asian oxygen isotope of precipitation indicates reduced summer seasonality in regional climate and westerlies. *Proceedings of the National Academy of Sciences of the United States of America*, 117(26), 14745–14750. <https://doi.org/10.1073/pnas.1922602117>
- Clemens, S. C., Prell, W. L., & Sun, Y. (2010). Orbital-scale timing and mechanisms driving Late Pleistocene Indo-Asian summer monsoons: Reinterpreting cave speleothem $\delta^{18}\text{O}$. *Paleoceanography*, 25(4), PA4207. <https://doi.org/10.1029/2010pa001926>
- COHMAP members. (1988). Climatic changes of the last 18,000 years: Observations and model simulations. *Science*, 241(4869), 1043–1052. <https://doi.org/10.1126/science.241.4869.1043>
- Comas-Bru, L., Atsawaranunt, K., & Harrison, S. P., & SISAL working group. (2020). SISALv2: Speleothem Isotopes Synthesis and Analysis database version 2.0 [Dataset]. *NOAA Paleoclimatology Data Archive*. Retrieved from <https://www.ncei.noaa.gov/pub/data/paleo/speleothem/SISAL/>
- Comas-Bru, L., Rehfeld, K., Roesch, C., Amirnezhad-Mozhdehi, S., Harrison, S. P., Atsawaranunt, K., et al. (2020). SISALv2: A comprehensive speleothem isotope database with multiple age–depth models. *Earth System Science Data*, 12(4), 2579–2606. <https://doi.org/10.5194/essd-12-2579-2020>
- Ding, Y., Wang, Z., Zhu, Y., & Sun, Y. (2008). Inter-decadal variation of the summer precipitation in China and its association with decreasing Asian summer monsoon Part I: Observed evidences. *International Journal of Climatology*, 28(9), 1139–1161. <https://doi.org/10.1002/joc.1615>
- Erb, M. P., McKay, N. P., Steiger, N., Dee, S., Hancock, C., Ivanovic, R. F., et al. (2022). Reconstructing Holocene temperatures in time and space using paleoclimate data assimilation. *Climate of the Past*, 18(12), 2599–2629. <https://doi.org/10.5194/cp-18-2599-2022>
- Goldsmith, Y., Broecker, W. S., Xu, H., Polissar, P. J., deMenocal, P. B., Porat, N., et al. (2017). Northward extent of East Asian monsoon covaries with intensity on orbital and millennial timescales. *Proceedings of the National Academy of Sciences of the United States of America*, 114(8), 1817–1821. <https://doi.org/10.1073/pnas.1616708114>
- He, C., Liu, Z., Otto-Bliesner, B. L., Brady, E. C., Zhu, C., Tomas, R., et al. (2021b). Abrupt Heinrich Stadial 1 cooling missing in Greenland oxygen isotopes. *Science Advances*, 7(25), eabh1007. <https://doi.org/10.1126/sciadv.abh1007>
- He, C., Liu, Z., Otto-Bliesner, B. L., Brady, E. C., Zhu, C., Tomas, R., et al. (2021a). Hydroclimate footprint of Pan-Asian monsoon water isotope during the last deglaciation. *Science Advances*, 7(4), eabe2611. <https://doi.org/10.1126/sciadv.abe2611>
- He, C., Liu, Z., Otto-Bliesner, B. L., Brady, E. C., Zhu, C., Tomas, R., et al. (2021c). Deglacial variability of South China hydroclimate heavily contributed by autumn rainfall. *Nature Communications*, 12(1), 5875. <https://doi.org/10.1038/s41467-021-26106-0>
- Herzschuh, U., Cao, X., Laepple, T., Dallmeyer, A., Telford, R. J., Ni, J., et al. (2019). Position and orientation of the westerly jet determined Holocene rainfall patterns in China. *Nature Communications*, 10(1), 2376. <https://doi.org/10.1038/s41467-019-09866-8>
- Jiang, M., Han, Z., Li, X., Wang, Y., Stevens, T., Cheng, J., et al. (2020). Beach ridges of Dali Lake in Inner Mongolia reveal precipitation variation during the Holocene. *Journal of Quaternary Science*, 35(5), 716–725. <https://doi.org/10.1002/jqs.3195>
- Jiang, W., Guo, Z., Sun, X., Wu, H., Chu, G., Yuan, B., et al. (2006). Reconstruction of climate and vegetation changes of Lake Bayanchagan (inner Mongolia): Holocene variability of the east Asian monsoon. *Quaternary Research*, 65(3), 411–420. <https://doi.org/10.1016/j.yqres.2005.10.007>
- Jiang, W., Leroy, S., Yang, S., Zhang, E., Wang, L., Yang, X., & Rioual, P. (2019). Synchronous strengthening of the Indian and East Asian monsoons in response to global warming since the Last Deglaciation. *Geophysical Research Letters*, 46(7), 3944–3952. <https://doi.org/10.1029/2019gl1082084>
- Kutzbach, J. E., & Otto-Bliesner, B. L. (1982). The sensitivity of the African-Asian monsoonal climate to orbital parameter changes for 9000 years B.P. in a low-resolution general circulation model. *Journal of Climate*, 39(6), 1177–1188. [https://doi.org/10.1175/1520-0469\(1982\)039<1177:tsotaa>2.0.co;2](https://doi.org/10.1175/1520-0469(1982)039<1177:tsotaa>2.0.co;2)
- Liu, J., Shen, Z., Chen, W., Chen, J., Zhang, X., Chen, J., & Chen, F. (2020). Dipolar mode of precipitation changes between north China and the Yangtze River Valley existed over the entire Holocene: Evidence from the sediment record of Nanyi Lake. *International Journal of Climatology*, 41(3), 1667–1681. <https://doi.org/10.1002/joc.6906>
- Liu, Z. (2014). Chinese cave records and the East Asia Summer Monsoon. *Quaternary Science Reviews*, 208, 111–129.
- Liu, Z., Otto-Bliesner, B. L., He, F., Brady, E. C., Tomas, R., Clark, P. U., et al. (2009). Transient simulation of last deglaciation with a new mechanism for Bolling-Allerød warming. *Science*, 325(5938), 310–314. <https://doi.org/10.1126/science.1171041>
- Lüthi, D., M. L. F., Bereiter, B., Blunier, T., Barnola, J.-M., Siegenthaler, U., et al. (2008). High-resolution carbon dioxide concentration record 650,000–800,000 years before present. *Nature*, 453(7193), 379–382. <https://doi.org/10.1038/nature06949>
- Ning, L., Liu, J., & Wang, B. (2017). How does South Asian high influence extreme precipitation over eastern China? *Journal of Geophysical Research: Atmospheres*, 122(8), 4281–4298. <https://doi.org/10.1002/2016JD026075>
- Ning, L., Xing, F., Wu, F., Lei, L., & Liu, Z. (2025). Data for the paper: “Mega-tripolar Precipitation Change Accompanying Water Isotopes in Holocene Asian Monsoon Reanalysis” [Dataset]. *Zenodo*. <https://doi.org/10.5281/zenodo.14994949>
- Otto-Bliesner, B., Tomas, E. B. R., Liu, Z., & He, C. (2024). iTraCE [Dataset]. *Research Data Archive at the National Center for Atmospheric Research, Computational and Information Systems Laboratory*. <https://doi.org/10.26024/b290-an76>
- Pausata, F. S. R., Battisti, D. S., Nisancioglu, K. H., & Bitz, C. M. (2011). Chinese stalagmite $\delta^{18}\text{O}$ controlled by changes in the Indian monsoon during a simulated Heinrich event. *Nature Geoscience*, 4(7), 474–480. <https://doi.org/10.1038/ngeo1169>
- Peltier, W. R., Argus, D. F., & Drummond, R. (2015). Space geodesy constrains ice age terminal deglaciation: The global ICE-6G_C (VM5a) model. *Journal of Geophysical Research: Solid Earth*, 120(1), 450–487. <https://doi.org/10.1002/2014jb011176>
- Ran, M., & Feng, Z. (2013). Holocene moisture variations across China and driving mechanisms: A synthesis of climatic records. *Quaternary International*, 313–314, 179–193. <https://doi.org/10.1016/j.quaint.2013.09.034>
- Stebich, M., Rehfeld, K., Schlutz, F., Tarasov, P. E., Liu, J., & Mingram, J. (2015). Holocene vegetation and climate dynamics of NE China based on the pollen record from Sihailongwan Maar Lake. *Quaternary Science Reviews*, 124, 275–289. <https://doi.org/10.1016/j.quascirev.2015.07.021>
- Stevenson, S., Otto-Bliesner, B. L., Brady, E. C., Nusbaumer, J., Tabor, C., Tomas, R., et al. (2019). Volcanic eruption signatures in the isotope-enabled last Millennium ensemble. *Paleoceanography and Paleoclimatology*, 34(8), 1534–1552. <https://doi.org/10.1029/2019PA003625>
- Tabor, C., Otto-Bliesner, B., Brady, E., Nusbaumer, J., Zhu, J., Erb, M., et al. (2018). Interpreting precession driven $\delta^{18}\text{O}$ variability in the South Asian monsoon region. *Journal of Geophysical Research: Atmospheres*, 123, 5927–5946. <https://doi.org/10.1029/2018JD028424>
- Tardif, R., Hakim, G. J., Perkins, W. A., Horlick, K. A., Erb, M. P., Emile-Geay, J., et al. (2019). Last Millennium Reanalysis with an expanded proxy database and seasonal proxy modeling. *Climate of the Past*, 15(4), 1251–1273. <https://doi.org/10.5194/cp-15-1251-2019>
- Tierney, J. E., Zhu, J., King, J., Malevich, S. B., Hakim, G. J., & Poulsen, C. J. (2020). Glacial cooling and climate sensitivity revisited. *Nature*, 584(7822), 569–573. <https://doi.org/10.1038/s41586-020-2617-x>
- Wang, S., Lu, H., Liu, J., & J. F. W. (2007). Negendank. The early Holocene optimum inferred from a high-resolution pollen record of Huguangyan Maar Lake in southern China. *Chinese Science Bulletin*, 52(20), 2829–2836. <https://doi.org/10.1007/s11434-007-0419-2>

- Wang, Y. J., Cheng, H., Edwards, R. L., An, Z. S., Wu, J. Y., Shen, C. C., & Dorale, J. A. (2001). A high-resolution absolute-dated late Pleistocene Monsoon record from Hulu Cave, China. *Science*, 294(5550), 2345–2348. <https://doi.org/10.1126/science.1064618>
- Wen, Q., Liu, Z., Jing, Z., Clemens, S. C., Wang, Y., Yan, M., et al. (2024). Grand dipole response of Asian summer monsoon to orbital forcing. *npj Climate and Atmospheric Science*, 7(1), 202. <https://doi.org/10.1038/s41612-024-00749-4>
- Wen, X., Liu, Z., Chen, Z., Brady, E., Noone, D., Zhu, Q., & Guan, J. (2016). Modeling precipitation $\delta^{18}\text{O}$ variability in East Asia since the last Glacial Maximum: Temperature and amount effects across different time scales. *Climate of the Past*, 12(11), 2077–2085. <https://doi.org/10.5194/cp-12-2077-2016>
- Xiao, J., Xu, Q., Nakamura, T., Yang, X., Liang, W., & Inouch, Y. (2004). Holocene vegetation variation in the Daihai Lake region of north-central China: A direct indication of the Asian monsoon climatic history. *Quaternary Science Reviews*, 23(14–15), 1669–1679. <https://doi.org/10.1016/j.quascirev.2004.01.005>
- Xie, S., Evershed, R. P., Huang, X., Zhu, Z., Pancost, R. D., Meyers, P. A., et al. (2013). Concordant monsoon-driven postglacial hydrological changes in peat and stalagmite records and their impacts on prehistoric cultures in central China. *Geology*, 41(8), 827–830. <https://doi.org/10.1130/g34318.1>
- Xu, H., Goldsmith, Y., Lan, J., Tan, L., Wang, X., Zhou, X., et al. (2020). Juxtaposition of western Pacific subtropical high on Asian summer monsoon shapes subtropical East Asian precipitation. *Geophysical Research Letters*, 47(3), e2019GL084705. <https://doi.org/10.1029/2019GL084705>
- Yu, G., Harrison, S. P., & Xue, B. (2001). Lake status records from China: Data base documentation MPI-BGC Tech Rep 4 (p. 247).
- Yuan, D., Cheng, H., Edwards, R. L., Dykoski, C. A., Kelly, M. J., Zhang, M., et al. (2004). Timing, duration, and transitions of the last interglacial Asian monsoon. *Science*, 304(5670), 575–578. <https://doi.org/10.1126/science.1091220>
- Zhang, H., Griffiths, M. L., Chiang, J. C. H., Kong, W., Wu, S., Atwood, A., et al. (2018). East Asian hydroclimate modulated by the position of the westerlies during Termination I. *Science*, 362(6414), 580–583. <https://doi.org/10.1126/science.aat9393>
- Zhao, L., Ma, C., Wen, Z., Ye, W., Shang, G., & Tang, L. (2021). Vegetation dynamics and their response to Holocene climate change derived from multi-proxy records from Wangdongyang peat bog in southeast China. *Vegetation History and Archaeobotany*, 31(3), 247–260. <https://doi.org/10.1007/s00334-021-00852-z>
- Zhou, W., Song, S., Burr, G., Jull, A. J. T., Lu, X., Yu, H., & Cheng, P. (2007). Is there a time-transgressive Holocene Optimum in the East Asian monsoon area? *Radiocarbon*, 49(2), 865–875. <https://doi.org/10.1017/s0033822200042739>
- Zhou, W., Yu, X., Jull, A. T., Burr, G., Xiao, J., Lu, X., & Xian, F. (2004). High-resolution evidence from southern China of an early Holocene optimum and a mid-Holocene dry event during the past 18,000 years. *Quaternary Research*, 62(1), 39–48. <https://doi.org/10.1016/j.yqres.2004.05.004>
- Zhou, X., Sun, L., Zhan, T., Huang, W., Hao, Q., Wang, Y., et al. (2016). Time-transgressive onset of the Holocene Optimum in the East Asian monsoon region. *Earth and Planetary Science Letters*, 456, 39–46. <https://doi.org/10.1016/j.epsl.2016.09.052>
- Zhou, X., Zhan, T., Tan, N., Tu, L., Smol, J. P., Jiang, S., et al. (2023). Inconsistent patterns of Holocene rainfall changes at the East Asian monsoon margin compared to the core monsoon region. *Quaternary Science Reviews*, 301, 107952. <https://doi.org/10.1016/j.quascirev.2022.107952>
- Zhou, X., Zhan, T., Tu, L., Smol, J. P., Jiang, S., Liu, X., et al. (2022). Monthly insolation linked to the time-transgressive nature of the Holocene East Asian monsoon precipitation maximum. *Geology*, 50(3), 331–335. <https://doi.org/10.1130/g49550.1>
- Zhu, C., Ma, C., Yu, S., Tang, L., Zhang, W., & Lu, X. (2010). A detailed pollen record of vegetation and climate changes in Central China during the past 16,000 years. *Boreas*, 39(1), 69–76. <https://doi.org/10.1111/j.1502-3885.2009.00098.x>
- Zhu, F., Emile-Geay, J., Hakim, G. J., Tardif, R., & Perkins, A. (2021). LMR Turbo (LMRt): A lightweight implementation of the LMR framework (0.8.0) [Software]. *Zenodo*. <https://doi.org/10.5281/zenodo.5205223>

References From the Supporting Information

- Coplen, T. B., Kendall, C., & Hopple, J. (1983). Comparison of stable isotope reference samples. *Nature*, 302(5905), 236–238. <https://doi.org/10.1038/302236a0>
- Huang, X., Pancost, R. D., Xue, J., Gu, Y., Evershed, R. P., & Xie, S. (2018). Response of carbon cycle to drier conditions in the mid-Holocene in central China. *Nature Communications*, 9(1), 1369. <https://doi.org/10.1038/s41467-018-03804-w>
- Rao, Z., Li, Y., Zhang, J., Jia, G., & Chen, F. (2016). Investigating the long-term paleoclimatic controls on the δD and $\delta^{18}\text{O}$ of precipitation during the Holocene in the Indian and East Asian monsoonal regions. *Earth-Science Reviews*, 159, 292–305. <https://doi.org/10.1016/j.earscirev.2016.06.007>
- Xu, H., Song, Y., Cao, J., Lan, J., Zhang, J., Zhou, K., et al. (2024). Heterogeneity of the East Asian rainfall influenced by solar-forced western Pacific subtropical high. *Communications Earth & Environment*, 5(1), 521. <https://doi.org/10.1038/s43247-024-01660-9>